

## ARTICLE OPEN



## Flexible active antenna arrays

Matan Gal-Katziri<sup>1,2</sup>✉, Austin Fikes<sup>1</sup> and Ali Hajimiri<sup>1</sup>

Complex and dynamic control of radiated fields are advantageous for flexible radio systems, which naturally move, roll, bend, twist, deform, and vibrate. Practical challenges hinder the proliferation of these antenna arrays. This work shows how using radio-frequency microchips reduces system component count, decreases mass to  $\sim 0.1 \text{ g cm}^{-2}$ , and increases functionality and mechanical flexibility. We develop a general platform for large scale flexible arrays and demonstrate two different 256-elements,  $30 \times 30 \text{ cm}^2$  flexible arrays. By varying supply distribution methods and radiators we show how performance can be optimized for maximum power delivery or physical flexibility. The demonstrated systems conform to curved surfaces with radii of curvatures as low as 23 cm and wirelessly deliver  $\sim 80 \text{ mW}$  of DC power to a  $6.7 \text{ cm} \times 11 \text{ cm}$ -receiver over one meter away. This paves the way towards the integration of smart arrays in flexible wearables and deployable lightweight airborne systems.

npj Flexible Electronics (2022)6:85; <https://doi.org/10.1038/s41528-022-00218-z>

## INTRODUCTION

Radio-frequency systems, and phased arrays in particular, are the next natural frontier of flexible platforms. Although phased arrays have been known at some level for more than a century<sup>1</sup>, their first applications can be traced back to aircraft detection radar and early telecommunication systems created prior to the second World War<sup>2–4</sup>. Constructive and destructive interference enables the concentration of power and a subsequent increase in gain and spatial selectivity for an array of microwave radiators<sup>5</sup>. Early works leveraged this phenomenon to create high gain, fixed direction arrays<sup>6,7</sup>, or create frequency scanning radiators<sup>8,9</sup>. As more complex circuits and systems emerged, systems which dynamically adjust the phase and amplitude of the excitation of each radiator, and thereby create electronically steerable beams, became more common. The first of these steerable phased arrays were bulky arrays constructed from discrete components<sup>4,10,11</sup>. Eventually monolithic microwave integrated circuits, based on compound semiconductors (e.g., GaAs), began to reduce the size of phased array implementations<sup>12,13</sup>. Beginning in the 1970s<sup>14</sup>, silicon integrated circuits began a march of progress that has led to their complete domination of digital electronics and nearly complete domination of lower-frequency analog electronics. Radio-frequency (RF) electronics remained unconquered by silicon until around the turn of the millennium, when silicon low noise amplifiers<sup>15</sup>, power amplifiers<sup>16</sup>, phase shifters<sup>17,18</sup>, synthesizers<sup>19,20</sup>, and then complete systems<sup>21–23</sup> emerged. After several more years of maturation, RF integrated circuit (RFIC) based phased arrays now form the foundation of 5G systems<sup>24</sup>.

Modern phased arrays or ‘smart antennas’ still rely on the same basic principles of operation: constructive interference created through independent control of the phase and the amplitude of each of the array’s elements. However, sophisticated digital control circuitry enables a plethora of capabilities, including beam focusing<sup>25</sup>, rapid beam steering, simultaneous multi-beam control<sup>26,27</sup>, and null synthesis<sup>28–30</sup>. These capabilities come at the cost of increased complexity. Element phase shifters should provide full  $360^\circ$  control, be linear, consume little DC power, and behave predictably and reliably in the face of mass-fabrication and environmental variations. If the phase shifters are used to

modulate digital data, both high resolution and rapid re-programmability are desired. If analog data is to pass through the phase shifter it must also be high bandwidth<sup>31,32</sup>. Amplitude modulation introduces additional concerns about power amplifier efficiency, linearity<sup>33</sup>, and tolerance of high peak-to-average power ratio (PAPR) signals<sup>34</sup>. For arrays that span beyond several dozens of elements, there are also system integration challenges of timing synchronization and data distribution that emerge from the increased board-level routing density<sup>35</sup>. Despite those issues, phased arrays are the primary solution in today’s transceivers thanks to their enormous functional versatility, non-mechanical control, and in the case of RFIC-based arrays, cost scaling and mass-production capabilities.

Flexibility introduces further complications in antenna design and reference distribution as well as position and orientation uncertainty for the element radiators during beam-forming. However, flexible and lightweight antenna arrays are required for a variety of emerging microwave applications. Wireless power transfer from space<sup>36–38</sup>, for example (Fig. 1a), requires large aperture phased arrays, which can be compactly stored during launch and later deployed in orbit. Flexible smart antennas can also be useful as deployable communication relays for large events (concerts, conventions, etc), or disaster relief/emergency situations when existing infrastructure is damaged (Fig. 1b). *Flexibility and reconfigurability* are necessary for arrays attached to dynamic surfaces<sup>39–41</sup> or used in wearable applications (e.g., Fig. 1c, d). Despite their broad potential, phased arrays have not yet been used in flexible systems<sup>42–47</sup>. While several exciting flexible RF components, such as diodes<sup>48</sup>, transistors<sup>49</sup>, switches<sup>50</sup> and antennas, have been demonstrated, the realization of complete systems requires significant additional functionality, namely, power, data, and clock distribution; local system monitoring and reconfiguration; external interface; and beam-steering. As a result, many recently demonstrated applications rely on additional rigid hardware to demonstrate the desired system functions<sup>49,51</sup>, and RF designers have to avoid flexibility altogether and settle for flat, rigid profiles with  $\lambda/2$  separated radiators.

RFICs can be effective tools in the implementation of various complex flexible systems that rely on coherent addition of radio signals. In this paper, we present a platform that relies on a

<sup>1</sup>Department of Electrical Engineering, California Institute of Technology, Pasadena, CA 91125, USA. <sup>2</sup>Present address: School of Electrical Engineering, Ben-Gurion University, Be'er-Sheva 8443944, Israel. ✉email: [matangka@bgu.ac.il](mailto:matangka@bgu.ac.il)

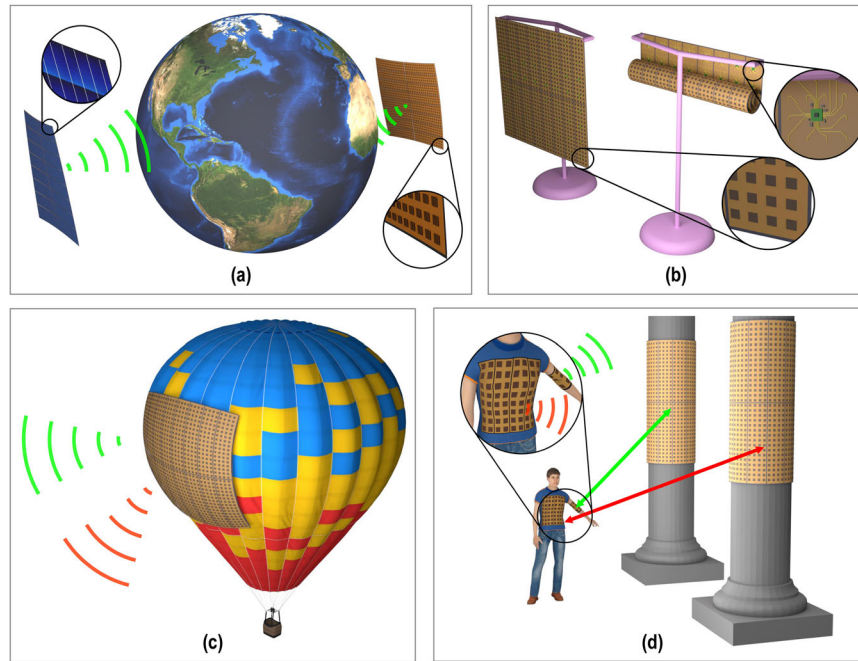


**Fig. 1** Example applications that are enabled by flexible smart antennas. **a** Lightweight deployable space structures. **b** Ad-hoc deployable antenna arrays. **c** Dynamic conformal surfaces. **d** Wearable conformal surfaces.

massive integration of system functions onto a single RFIC, to enable fully functional flexible phased arrays. The results section will present the flexible circuit platform and detail how our RFIC is utilized in this modular and decentralized architecture. We will discuss power and control distribution challenges and solutions, as well as calibration and focusing of large flexible arrays. These functions are essential to resolve the phase offsets in the system due to manufacturing variations, shape deformations, or environmental changes. We will present two practical implementations of 256-element flexible active transmitter antenna arrays, that maximize either specific power delivery or mechanical flexibility of the active array platform. These implementations constitute two functional demonstrations of *self-contained* large scale flexible active arrays.

## RESULTS AND DISCUSSION

### A scalable and modular flexible phased array platform

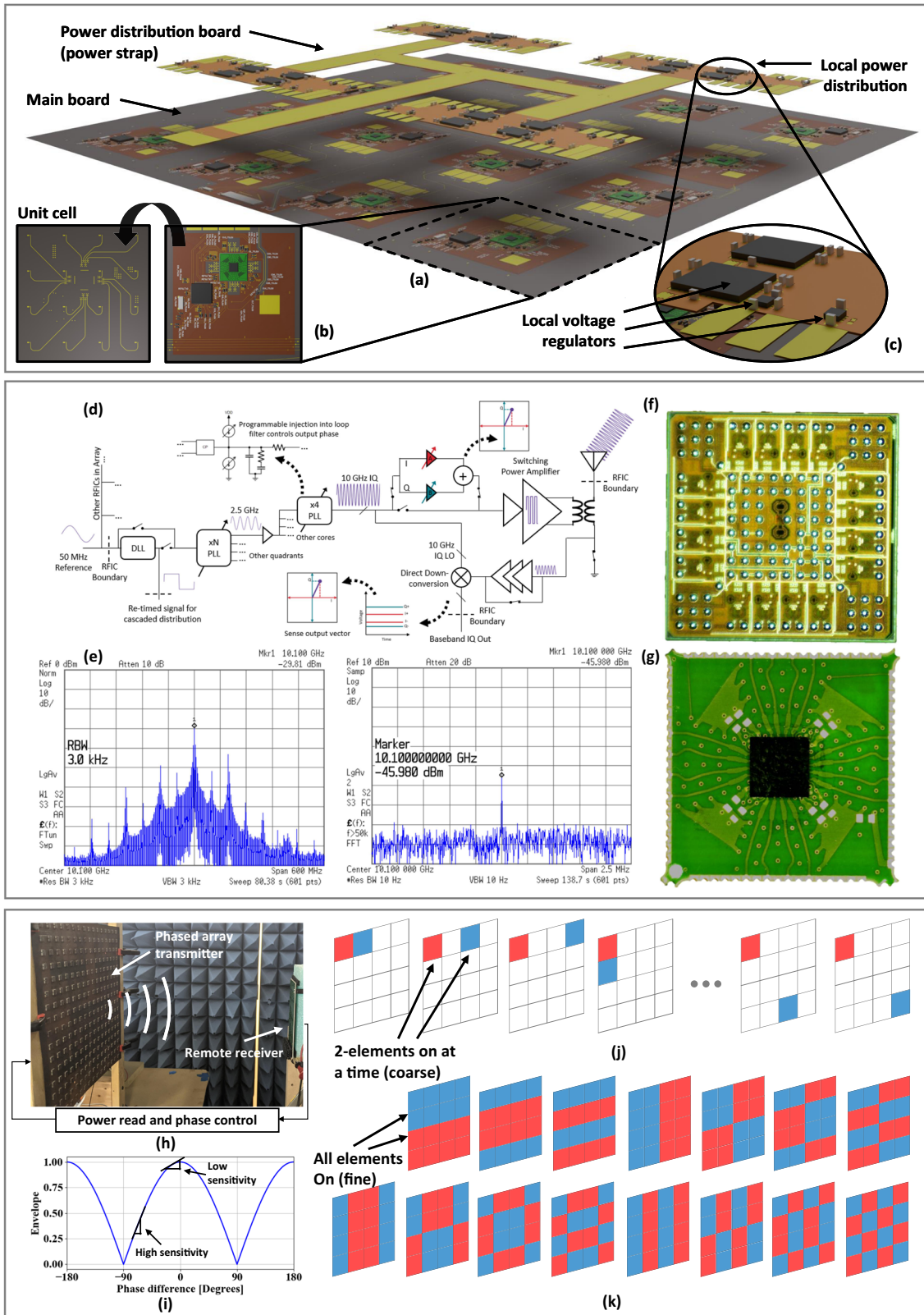
Our flexible array platform is illustrated in Fig. 2a. The primary structural component is a thin multi-layer flexible printed circuit board, later referred to as a flexible sheet. Antenna arrays rely on repeating patterns, and so the primary sub-unit is designed to be modular, each containing an RFIC capable of driving 16 radiators, a micro-controller unit (MCU) with non-volatile memory, several small decoupling capacitors, and accompanying wire traces. This modular sub-unit can be instantiated many times to fabricate large scale arrays of various sizes<sup>52</sup>. The use of an RFIC drastically reduces the component count compared to traditional design and thus enables mechanical flexibility. An H-tree clock distribution network synchronizes the RFICs to a central reference clock. Each sub-unit has its own power interface and can be powered in different ways (e.g., a shared global distribution network, local photovoltaic cells, etc.) based on the application. The 16 high-frequency radiator feed traces transition to the backside of each sub-unit (opposite to the RFICs) and drive a  $4 \times 4$  pattern of radiators, spaced  $0.6 \lambda$  (wavelength) apart, to improve channel-to-channel isolation (Fig. 2b). The mounting interface is designed to accommodate a variety of antenna types, as evident in the details of our two specific implementations. The flexible sheet is

fabricated using a Pyralux-AP<sup>53</sup> (polyimide) laminate by DuPont<sup>TM</sup>. It has a dielectric constant of  $\epsilon_r \approx 3.4$  and loss tangent of  $\tan(\delta) \approx 0.005$ , which are stable at RF, well-characterized, space grade, and with high-frequency (below 20 GHz) comparable to commercial rigid materials<sup>54</sup>. These characteristics permit the design of microwave structures with reasonable transmission line dimensions; a  $50 \Omega$  transmission line on a  $75 \mu\text{m}$  kapton substrate has a width of  $\sim 0.2 \text{ mm}$  and can be manufactured reliably. We use a 4-layer laminate which is the minimum required for the antenna traces, antenna ground layer, supply, and signal routing in our system. The design supports the use of a distributed power supply—for example local solar cells feeding each RFIC<sup>36–38</sup>—to reduce the ohmic losses in the power distribution lines and simplify the component-side design of the flexible sheet. It also supports the use of a centralized power source, distributed to the RFICs through a low resistance flexible board strap (Fig. 2c). To reduce ohmic losses a high-voltage power supply distribution scheme can be used, where it is stepped-down to the required supply voltage locally by high-efficiency DC-DC converters.

### Transmit array driver integrated circuit

The main building block of our flexible architecture is our custom designed silicon RFIC transmitter. It weighs a practically negligible 85 mg and provides 16 channels of phase-locked 10 GHz signals with individually, digitally controlled phase and amplitude, enabling the array to synthesize and steer custom beam patterns. Such level of complexity is impossible with discrete components with the given array sub-unit size, and is a critical enabler of flexible arrays.

A functional description of each channel of the RFIC is shown in Fig. 2d. The 10 GHz signals are synthesized from a 10–100 MHz reference in two stages; first a central phase-locked loop (PLL) with programmable division ratio generates a signal close to 2.5 GHz which is distributed to the circuitry of all the individual output channels, each called a core. At each core, a second, individual PLL stage synthesizes a 10 GHz signal from the 2.5 GHz reference. Two stage frequency synthesis relaxes requirements on signal distribution circuitry and provides an opportunity for phase control within each core. Full-360° phase control is achieved through



programmable current injection into the PLL loop filter. Figure 2e illustrate the power spectrum emitted from 256 radiators driven by 16 RFICs, in which the radiated output signal is accurately synthesized from a low frequency reference, and Fig. 2f is a photo of the IC die.

In addition to the essential signal synthesis and amplification functions, the chip possesses several features. Volatile memory cells control the weights of a vector sum phase rotator which can be bypassed for low power operation or used to enable rapid time multiplexing of the beam direction. Two of the 16 channels



**Fig. 2 An implementation of a modular, flexible phased array platform.** **a** The multi-layer flexible sheet is designed from multiple **b** sub-unit patterns. Each sub-unit accommodates a 16-channel RFIC array transmitter driver, a micro controller, and filtering capacitors. On its back side there are fan-out transmission lines for 16 antenna mounts. **c** Power can be delivered by a separate low-cost flexible strap and converted to the required voltage levels near each array sub-module. **d** Functional diagram of RFIC. **e** Wide bandwidth and narrow bandwidth measurements of the radiated output power spectrum of the array at  $\sim 1$  m. **f** Micrograph of RFIC. **g** RFIC mounted on interposer. **h** A test setup with a smart antenna and remote receiver that form a feedback system for a focusing algorithm. **i** The fundamental problem of reduced sensitivity near optimum phase combining, exemplified by a coherent addition of two sinusoidal wave-forms. **j** Initial focusing of smart array of radiator pairs. The quality of focusing depends, among other things, on the receiver dynamic range, which cannot sense phase changes near optimum phase combination. The limitations are overcome by performing additional phase combination over groups of several arrays. **k** At the limit, half of the array radiator phases can be swept with respect to the other half, and thus increase the power variation at the receiver.

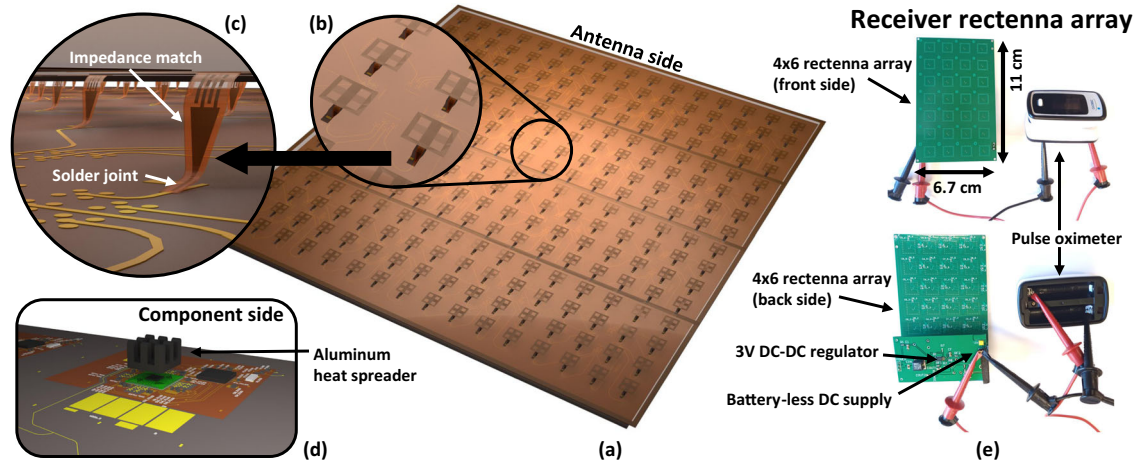


**Fig. 3 Antenna sheet structure.** **a** This single layer antenna sheet is assembled on the back side of the base-design multi-layer flexible sheet. **b** Printed antenna patterns and **c** antenna feed assembly. **d** Aluminum heat-spreaders. **e** Power receiver board with an example consumer device (a commercial pulse-oximeter) attached to it.

possess self-sensing receivers which have been co-designed with the power amplifier, similar to<sup>55</sup>. These parasitic receivers can be used to perform reflection sensing for phase calibration and shape estimation purposes. To achieve high on-chip circuit density for the transmitters, a non-resonant inductorless receiver architecture is adopted. The receiver chain has an overall (RF to baseband) noise figure of 10 dB, which is sufficient for its intended calibration operations and does not sacrifice the integration density or performance of the transmit circuitry. On-chip current, voltage, and temperature sensors provide system health and environmental monitoring. Important RFIC block- and system-level performance measurements are presented in the methods section. Integrated circuits are difficult to mount directly to flexible circuit boards, which typically have more strict design-for-manufacturing rules<sup>56</sup> than conventional printed circuit boards, where excessive bending can result in reliability issues. Consequently, the RFICs are mounted on interposers (Fig. 2g), which also provide the trace fan-out necessary for interfacing with fine pitch bumps. The interposers are fabricated using a 4 layer 1 cm x 1 cm substrate board and are small enough not to limit the bend radius of the larger array.

### Array Focusing

A challenge for these arrays is that RF phase of the signal at each radiator is initially deterministic, yet unknown, and varies from one element to the next. This can be due to static fabrication and assembly variations between TX/RX channels, or dynamic effects such as temperature changes or mechanical vibrations. To resolve the phases of the signals emitted from the radiators in our arrays, we use closed-loop feedback from a remote receiver, as shown in Fig. 2h. The focusing method is discussed thoroughly in<sup>25</sup>, where a multidimensional variable-dynamic-range search algorithm is designed to work at an arbitrary distance from the antenna plane (As opposed to array calibration, which usually refers to focusing

to a focal point at infinity, i.e. in the far field). This algorithm solves a major challenge in high-power arrays: as the phase settings approach the desired optimum to point to a target, the effect of changing the phase of a single element decreases (Fig. 2i). This sets severe dynamic range requirements on the focusing feedback receiver, which must handle diminishing power variation towards the end of the process. With our method, focusing starts with simultaneously varying the phases of small subsets of array elements. At this point, power readings are large and coarse tuning is achieved (Fig. 2j). As the phase variations become smaller in later iterations, we increase the number of simultaneously phases-varying elements. This increases power variations at the receiver and consequently the dynamic range, and provides fine tuning of the array (Fig. 2k). An adaptive orthogonal basis is created to guarantee full spanning of the parameter space.

### A lightweight, high power flexible phased array transmitter

The first realization of the flexible phased array platform optimizes the specific power (radiated-power-to-mass ratio) of the array. This objective is beneficial to lightweight airborne systems such as drones, small satellites, and space-based power (SBP)<sup>37</sup> systems, in which the antenna weight comes at the expense of other functionality, or affects the economical viability of the system. The design uses a single 25  $\mu\text{m}$  thick polyimide sheet with 256 air-gap dielectric patch radiators etched into a copper layer (Fig. 3a, b). The air gap minimizes substrate losses and provides wide-band matching compared to conventional dielectric patch antennas<sup>57</sup>. Each radiator's conductive area is further reduced by subtracting small squares from the patch copper surface. The smaller footprint reduces coupling between radiators to below  $-15$  dB and decreases the overall metal content. Radiator feeds are cut out from the antenna sheet and the radiator array sheet is held taut by a lightweight glass fiber frame providing structural integrity. The antenna sheet is assembled on the multi-layer flexible sheet by



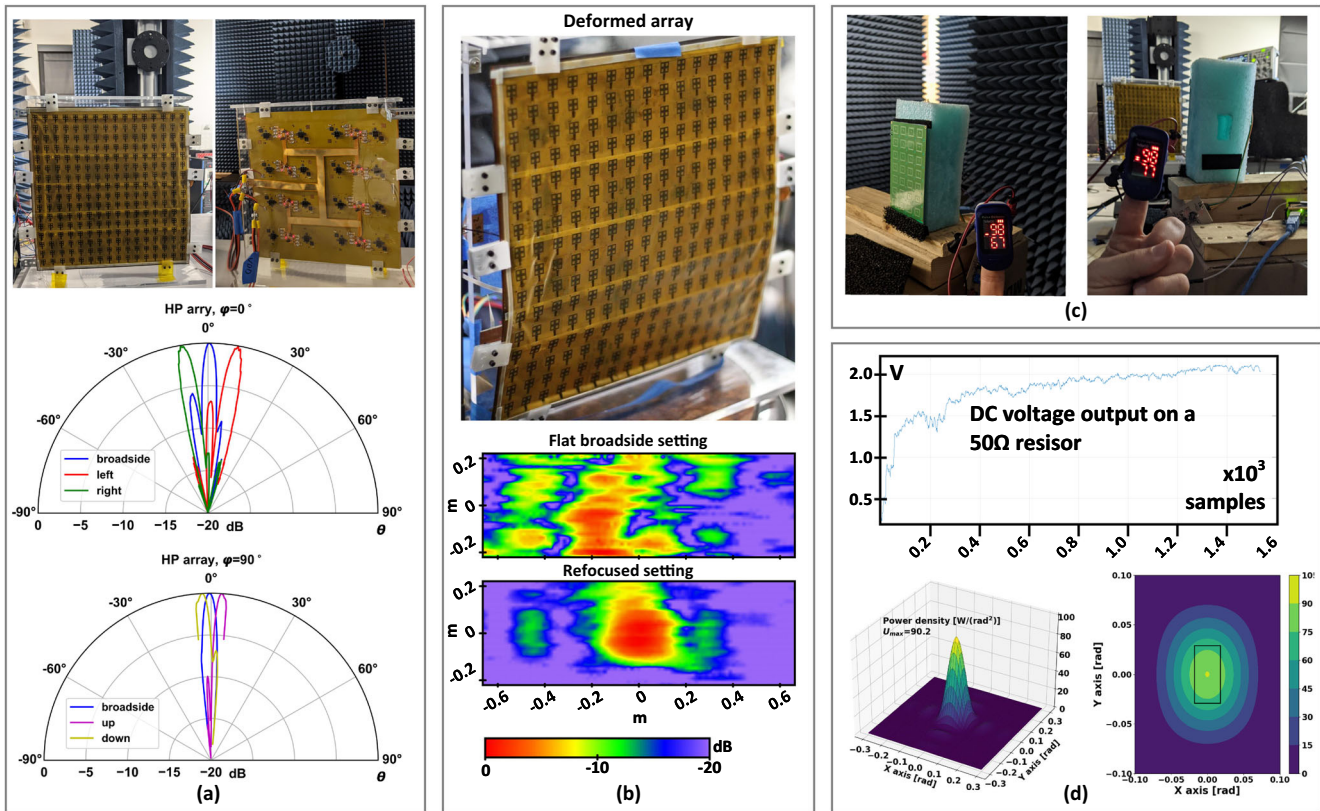


**Fig. 4** Antenna sheet array measurements. **a** Beam-steering, **b** deformation correction, **c** RF-DC wireless power transfer of about 80 mW at 1 m away from the transmitter to a small rectenna array. **d** Measured output voltage on a  $50\ \Omega$  resistor, 1 m away from the array (top), angular power density (bottom-left) and expected power delivery distribution to the remote receiver at  $\sim 1.6$  m away from the array (bottom-right).

first soldering the feeds to the carrier board transmission lines and then lifting the radiator sheet such that the antenna feeds rise from the transmission lines on the carrier board (Fig. 3c). Small glass fiber springs or supports then hold the antenna sheet deployed while providing some movement flexibility that relieves structural stress.

This design is intended to work with a distributed power supply from local solar cells to each array sub-unit<sup>36,37</sup>. However, distributed photovoltaic supplies are poorly suited to laboratory characterization of the array. As such we use a low resistance flexible board strap as a surrogate for local power generation. A nominal 1.8 V is supplied from a central source to each of the RFIC's four PA quadrants. The DC supply is also converted to 1.2 V by a linear regulator for the rest of the IC circuitry, and to 3.3 V by a voltage doubler to power the sub-module MCU. These additional regulators are miniature (about  $4\ \text{mm}^2$  each) and do not contribute much to the overall area or power consumption of the system. Performance is characterized in a terrestrial lab rather than in the intended, much colder space environment. To handle the higher temperatures of testing conditions we attach a commercial aluminum heat-sink with a thermal resistance of  $32\ ^\circ\text{C}\ \text{W}^{-1}$  on top of each IC, which can typically dissipate 3.7 W from a  $14\ \text{mm}^2$  area of 0.3 mm thick silicon die (Fig. 3d). The result is a high power and low mass radiating array, with a 2-D phase steering and deformation correction capability, that can radiate up to 0.8 W at a distance of 2 m away from the antenna surface. A small array of  $4 \times 6$  10 GHz tuned rectennas<sup>58</sup> (Fig. 3e) is used as a receiver to focus the beam pattern using the closed-loop procedure described above. Measured antenna patterns are illustrated in Fig. 4a. The antenna performance was characterized in an automated test range<sup>59</sup> with fields measured at a distance of 2 m away from the radiators plane, as detailed in the methods

section. The azimuth and elevation broadside radiation patterns are similar to the analytical approximation for large arrays<sup>25</sup>. Steering angles of  $\pm 10^\circ$  azimuthal and  $\pm 3^\circ$  in elevation are demonstrated, constrained by the test setup limits. The measured half-power beam width (HPBW) is on average  $5^\circ$  with a standard deviation of 0.61°, and is in a good agreement with the expected value of  $5.2^\circ$ <sup>60</sup>. The measured location of the first null of radiation pattern is  $\sim 5.5^\circ$  from the lobe center and is in a good agreement with the expected value of  $6^\circ$ , for  $N(d/\lambda \cdot \pi) \cdot \sin\theta = \pi$ , and radiators at a distance  $d = 0.6\ \lambda$  from each other. EIRP is estimated by normalizing the main lobe height to contain the measured 0.8 W. This results a radiation intensity of  $90.2\ \text{W}\ \text{rad}^{-2}$ , which translates to an effective isotropic power of  $\sim 60.5\ \text{dBm}$ . This result is in line with an initial estimate of 63 dBm EIRP that assumed  $\sim 15\ \text{mW}$  channel output power, cable loss of 3 dB, and 256 radiators with a combined directivity of 30.6 dB. The EIRP difference can be explained from the measured radiation pattern that shows higher-than-expected side lobes at  $-7\ \text{dB}$  below the main lobe, which may occur due to imperfect focusing. This conclusion is supported by a calculation of directivity using our antenna range setup, of which result was 26.5 dBi due to the residual side lobes. The measured radiation patterns are in general similar to the expected analytical results. One reason for elevated side lobes in some of the patterns is that the array was focused to a target in the near field, due to size constraints of the antenna measurement setup. This can lead to multi-path reflections having been used by the focusing process to maximize power, which can later manifest as raised side-lobes after conversion to the far field. Measurements that are different from the analytical result can also be due to optimizing the power transmitted to a single receiver. The used focusing algorithm is oblivious to the radiated field at any location other than at the receiver. Hence noise, radiator

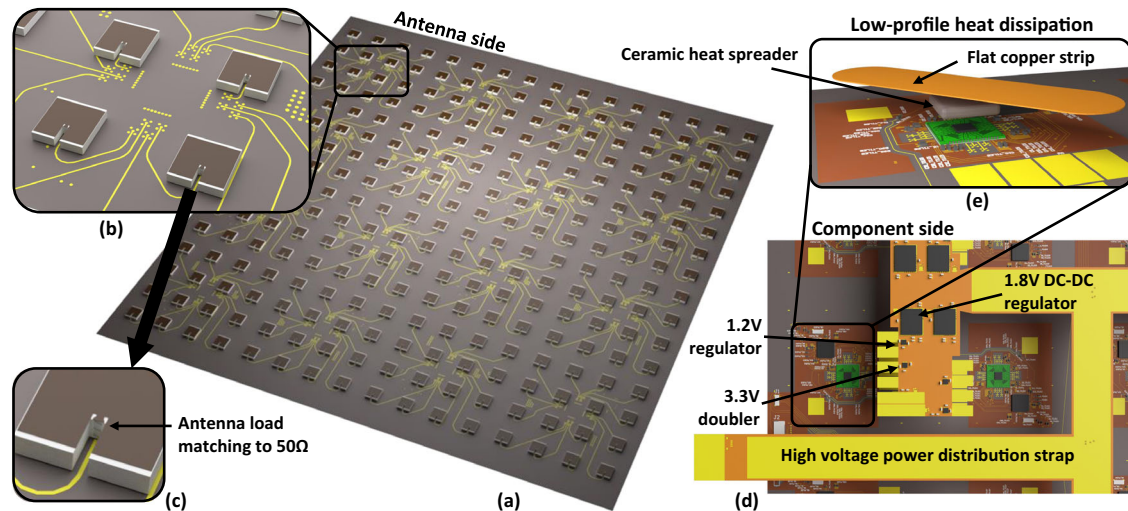


**Fig. 5 Flexible and robust active antenna design.** **a** Flexible sheets boards with **(b)** Discrete patch antennas. **c** The antenna feed via is used for impedance matching. **d** High voltage (up to 6 V) power delivery strap with local voltage regulator. **e** Low-profile heat spreaders.

power mismatch, or external disturbances, may result in algorithmic optimum with raised side-lobes. Such non-idealities in the radiation patterns can be alleviated by calibrating the arrays at a properly sized facility in the large-scale manufacturing phase. In addition, it may be beneficial to integrate additional calibration features in the RFIC, as sometimes done to evaluate patterns and perform on-site calibration in rigid phased arrays<sup>61–66</sup>.

One potential use of our system is to wirelessly power remote instruments, such as vital sign monitors of isolated patients in a dynamic environment. This use case is especially relevant in current reality of a world-wide, airborne, viral pandemic, which requires medical crews to continuously treat and monitor quarantined patients. We use our 6.7 cm × 11 cm receiver rectenna in conjunction with a 3.3 V DC-DC converter module to power a commercial 60 mW pulse oximeter in *real time*, as shown in Fig. 4c, without the need for additional batteries. The measured power distribution in the main lobe is used to estimate the maximum distance at which the oximeter will be powered. The rectenna peak efficiency of 45% at 10 GHz<sup>58</sup> and the DC-DC converter efficiency of 60–80% (Efficiency is input power dependent) predict a usable range of 1.57 m–1.89 m away from the transmitter. In practice, we achieved a maximum operating range of ~1 m where we measured RF to DC power transfer of about 80 mW (Fig. 4d). It is likely that sub optimal rectifier efficiency and high startup power draw prevent the oximeter from turning on at a larger distance.

The high-power active array is lightweight and efficient. The low-voltage supply makes it suitable for distributed local power supply. By using elastic antenna sheet separators, the structure can be stored with the antenna sheet flattened against the multi-layer flexible sheet, then later deployed for use. The drawback of this implementation is limited flexibility—only up to the radial mismatch between the antenna sheet and the flexible sheet, and physical strength of the thin antenna leads that connect between the two.

#### A dynamically flexible or conformal phased array transmitter

To overcome the radial bending limitations of the high-power array, we have designed a *second* prototype with significantly enhanced flexibility and structural robustness, at the cost of reduced output power. Highly flexible antenna sheets are important for small curvature carriers like miniature UAVs, for deployable applications where the array should be rolled back to its storage configuration after use, and for highly dynamic wearable systems. Flexible arrays can also be used as traditional

conformal systems on a variety of surfaces without requiring changes to the design or manufacturing process.

The second array shown in Fig. 5a adopts discrete dielectric patch antennas that are assembled individually onto the base-design flexible sheet, so they do not significantly limit its bend radius. This enables to reduce the size of the antennas at the cost of performance as detailed in the methods section. Several approaches exist to increase the bandwidth of patch antennas<sup>67,68</sup> and to reduce the size of low-dielectric radiators<sup>69,70</sup>, but in our proof-of-concept we use a traditional design (Fig. 5b, c), where the feed and landing-pad form an equivalent LC impedance conversion circuit to match the antenna impedance to the feeding transmission line. This highly flexible prototype is designed to demonstrate operation from a centralized supply like a battery or AC mains. We distribute up to 6 V along the array (Fig. 5d), and use a commercially available switching regulator for the conversion to the local 1.8 V unit. As a result, the resistive loss of the DC supply lines is reduced by a factor of 3 compared to the high-power array that was presented previously. The supply line remains thin enough to not limit the array movement. The distributed 6 V is generated from a standard 20 V laptop power brick using a 125 W capable commercial miniature DC-DC converter. The last variation to this second enhanced-flexibility design is a replacement of the tall aluminum heatsinks with a low profile solution. We assembled flat ceramic heat spreaders on top of the RFICs and covered each of the spreaders with a 165 μm thick, 40 mm × 15 mm copper strips to conduct heat away (Fig. 5e). The use of flat and bendable heat conductors enables the array to conform to curved surfaces such as airplane bodies, where the carrier surface itself participates in the heat conduction away from the chips. The low profile is also more inline with wearable devices requirements.

The array can be bent in the horizontal and vertical dimensions with concave and convex radii <23 cm, and remain fully functional and programmable with focusing, pattern recovery, and 2-D beam steering capabilities. The maximum demonstrated steering angle of ±10° and focusing range—1.6 m at the moment—are limited by the antenna range dimensions. Far-field patterns are obtained from a mathematical conversion of the near-field measurement<sup>59</sup>. As a result there are small differences in lobe direction compared to the near-field target location. Figure 6a shows a beam pattern that closely follows the simulation of a 256-element array, with a broadside HPBW of 5.6°. When flat, the average HPBW of the antenna is 5.6°,  $\sigma = 0.7^\circ$  compared to expected 5.2°. Directivity of ~26.5 dBi was calculated from the far field pattern, similarly to the first antenna prototype. When the antenna is convex and concave



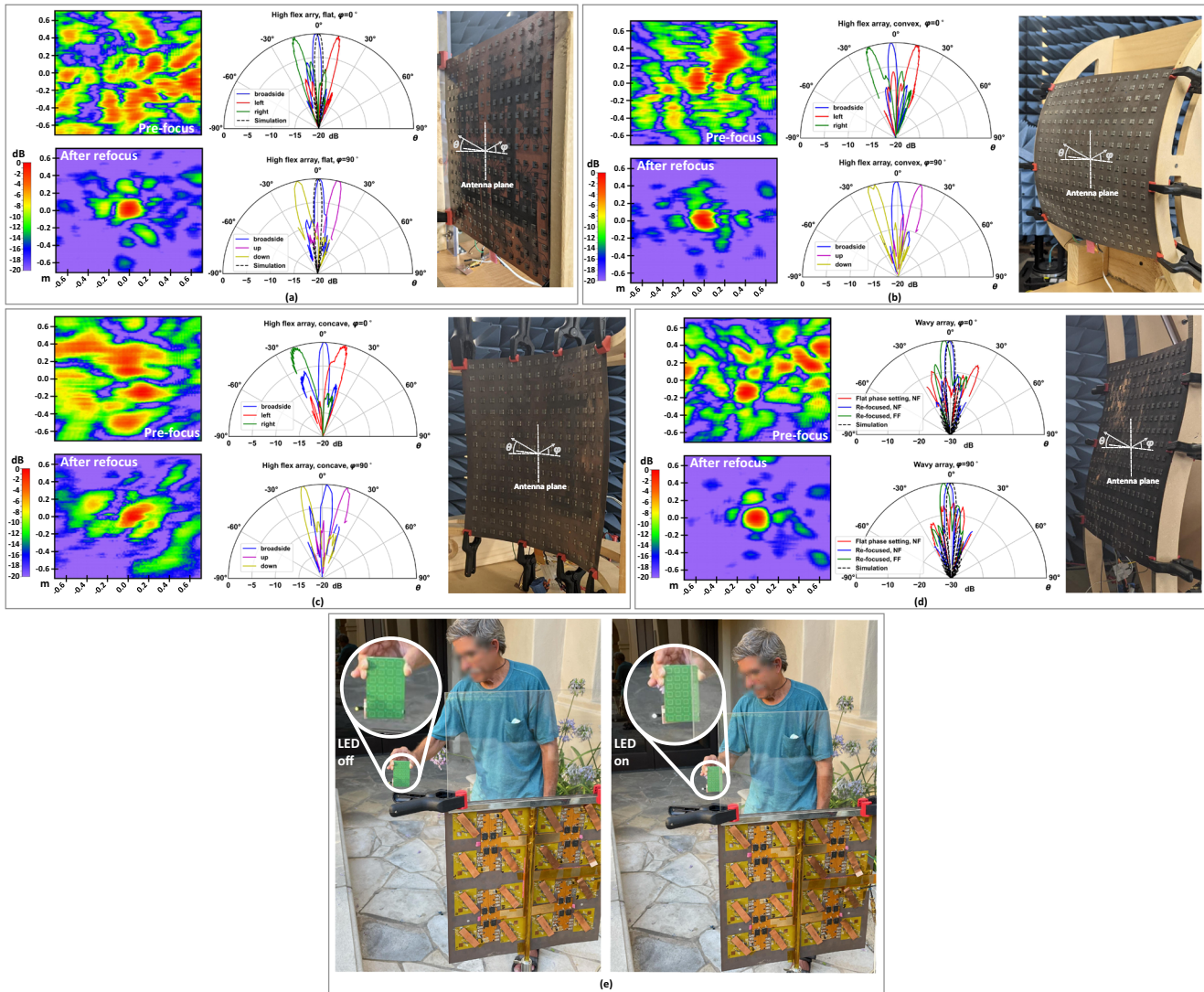


**Fig. 6 Flexible array measurements, demonstrating bend radii <math>< 23\text{ cm}</math>.** Figures a–d include pre- and post-focusing 2-D near-field radiation patterns (left), beam-steering of the main lobe (center), and array formation (right). **a** 2-D beam-steering with flexible array in planar configuration. **b** 2-D beam-steering with flexible array in convex configuration. **c** 2-D beam-steering with flexible array in concave configuration. **d** 2-D beam-steering with flexible array conformed to a doubly curved shape. **e** Outdoor deployment and focusing to power an LED indicator. The LED is on when the receiver is at the focus point (right) and off when moved away from it (left).

(Fig. 6b and c) broadside-focused lobes are with an HPBW as expected, but the steered lobes are affected by bending, with average HPBW of  $6.4^\circ$  and  $6.7^\circ$ , respectively. This is partly the result of increased non linear coupling effects between neighboring synthesizers and between neighboring power amplifiers that drive each radiator. Such coupling cannot be accounted accurately by the iterative focusing process. In addition, the short range focusing results beam widening after the pattern is transformed to far-field, and sampling effects cause ripples near the phase scan boundaries. For a comparison, HPBW of the raw, *near-field* radiation patterns at the focusing distance, is  $5.6^\circ$ ,  $5.1^\circ$ , and  $5.9^\circ$  for flat, convex, and concave bends, respectively. It is noteworthy that bending the antenna results lower transmitted power compared to a flat configuration. The receiver rectenna voltage after focusing is lower on average by 10% and 24% in convex and concave bends, respectively, indicating average power density decrease of 0.95 dB, and 2.3 dB, respectively. In a follow-up mixed experiment we bent the flexible array to a doubly curved shape and directed it at an angle from the receiver. Figure 6d illustrates how focusing can correct the radiation pattern under a physical

deformation. After refocusing, the receiver voltage is only 0.3 dB lower than the value obtained from flat broadside optimization—within measurement tolerance. Worst case side lobes in our steering experiments are at about  $-7\text{ dB}$  and are a mostly a results of reflections due to near-field focusing. Figure 6d also illustrates how the mathematical near- to far-field conversion results a deviation of the lobe center from the near field pointing direction. While this is not a fundamental problem, it highlights the importance in understanding the geometric properties of array focusing. Like the high-power implementation, this array is also capable of powering a remote pulse oximeter, but at a reduced distance of 40 cm away from the radiator. The reduction in power delivery range implies a reduced EIRP of the flexible implementation to  $\sim 52\text{ dBm}$  compared to the high-power light-weight antenna. The estimated EIRP value was verified by a direct measurement. The dielectric patch array was focused at a target at 6.2 m just beyond the far-field threshold of 6 m. Accounting for path loss, transmission at  $\sim 10\text{ GHz}$  and a horn antenna with a known receiver gain of 11 dBi, the measured EIRP is 52.7 dBm. The reduced EIRP is a result of the design choice to optimize flexibility



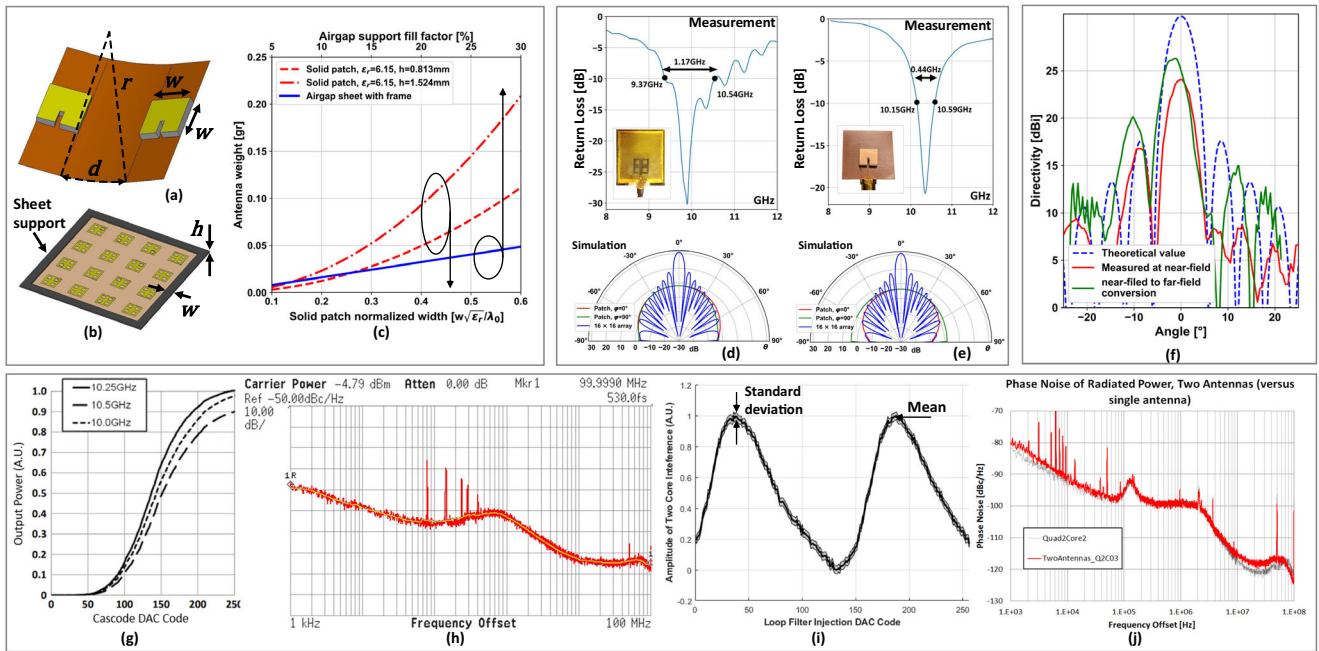


**Fig. 7 Measurement and design details.** **a** Dielectric patch antenna structure and implication on flexibility and **b** air gap patch and dimensions of glass fiber support. **c** Antenna mass as a function of dimensions, or support fill-factor. Matching and radiation patterns of **d** air gap and **e** dielectric patch radiators. **f** Measured directivity of near- and far-field patterns compared to analytical value. **g–j** Show RFIC functionality. **g** Normalized cascode amplitude control at three frequencies. Re-used with permission from<sup>75</sup>. **h** Signal spectrum. Re-used with permission from<sup>25</sup>. **i** Radiative measurement of interference pattern demonstrating independent phase control of driver cores within the same current-sharing stack. Mean and standard deviation of ten trials plotted. **j** Radiative phase noise measurement of one core and two cores.

and robustness at the expense of raw transmission power. However, the enhanced robustness enabled us to deploy the flexible array outdoors and demonstrate beam focusing at a building entrance about, 1.5 m away from the antenna surface. After refocusing, the deployed array delivered enough power to a receiver to light a high-power indicator LED (Fig. 6e), proving its functionality in the field.

## METHODS

### Design details

Complete large-scale flexible RF electronics systems are enabled by several design choices. Most importantly, discrete component count is reduced by the use of a single RFIC. As such, RFICs must be implemented in a process technology that supports a sufficiently high level of integration. In our work we use a standard bulk-CMOS 65nm process, which balances a high cutoff frequency of  $f_t > 130$  GHz, a relatively wide range of supply voltages (1 V core, 3.3 V I/O), and low cost—an important parameter for large-scale systems. The chip assembly interface utilizes die bumps (flip-chip technology) with a pitch of 175  $\mu\text{m}$ , as opposed to bond-wires, in order to reduce RF interface parasitics and increase the I/O density. The RFIC is soldered onto a 1  $\text{cm}^2$ , 0.4 mm thick, 4-layer rigid carrier board (interposer). The interposer top two layers share a high frequency RO4350B core material and are used for RF I/O distribution. The bottom metal layers share an FR4 core and are used for supplies and low-frequency control signals. Four small 8 cm fans were deployed behind the multi-layer flexible sheet for better thermal control during the evaluation of the flexible system. Each RFIC is controlled by an Atmel SAMD21 MCU. An off-board programming interface to these microcontrollers has been implemented with both serial and parallel control. The serial control configuration uses a shared SPI bus with each microcontroller given an address. The parallel control uses as individual SPI buses to each microcontroller, driven by an FPGA. The control configuration

can be changed by populating/depopping jumper resistors on the flexible sheet.

Differently from *conformal* antennas arrays, that are fabricated using a high frequency laminate and mounted onto a static, curved surface<sup>71</sup>, with no requirement that the system's electronics be nearby the radiators, truly *flexible* arrays like the ones presented here are expected to also be stored, deployed, and embedded in dynamic applications, e.g. wearables. Such features require the radiators and electronics to be mounted onto thin and lightweight carrier boards. The two arrays that we presented are fundamentally flexible substrates with cavity patch radiators. The first, high-power antenna uses 9 mm  $\times$  9 mm air-gap patches that are printed on a single-sided copper-clad Kapton layer. The Kapton and copper thicknesses are 25  $\mu\text{m}$  and 34  $\mu\text{m}$ , respectively. The thin antenna sheet needs additional support to remain flat. This additional support can be quantitatively evaluated by fill-factor. We currently use glass-fiber with a mass density of  $\approx 2$  g  $\text{cm}^{-3}$  and 20% fill factor, which result an equivalent radiator weight of  $\approx 37$  mg. Our second, highly flexible antenna utilizes rigid 6.9 mm  $\times$  6.9 mm patches, designed on a 2-layer, 1.27 mm-thick Rogers RO3006<sup>®</sup> laminate, with  $\epsilon_r \sim 6.15$ . Smaller patches enable a smaller bend radius, depending on the multi-layer flexible sheet substrate materials and dimensions (7a). The mass of each patch is calculated assuming a mass density of 2.6 g  $\text{cm}^{-3}$ <sup>72</sup> to be  $\approx 100$  mg. Figure 7b, c show how radiator weight changes with the selection of fill factor in air-gap radiators and with the size of dielectric patches. In most cases, the mass of air gap radiators is significantly lower. In addition, the radiating field density is higher in dielectric patches, which results increased loss and decreased antenna bandwidth<sup>57,73</sup>. Despite their drawbacks, the discrete patches fundamentally enable the system flexibility and therefore they are used in our second, highly flexible array. Both types of patch radiators are matched around 10 GHz (Fig. 7d, e), and are simulated to perform similarly in our 256-element arrays.

While the presented integrated circuit based flexible arrays operate at 10 GHz, the frequency of operation can be increased or

decreased over a wide range without fundamental changes to the design architecture. Arrays at lower frequencies can operate with similar electronics and radiator technology although the radiating elements may need to be mechanically strengthened when scaled up. Integrated circuit based arrays which radiate the fundamental signal frequency have been demonstrated beyond 100 GHz<sup>74</sup>. However, as array frequency increases, their size decreases. This decrease implies higher component density and increased substrate thickness relative to aperture size, both reducing flexibility. Further disincentive to pushing deep into mm-Wave frequencies is the practical consideration that small apertures are much more likely to fit on surfaces without needing flexibility. Rather than a hard upper frequency limit set by the electronics, there is a soft frequency limit above which flexibility is no longer a compelling attribute for a phased array.

### Measurement details

The presented arrays are large compared to the radiated wavelength: 30 cm × 30 cm. This results a 10 GHz far field limit,  $2D^2/\lambda$ , at about 6 m away from the radiator—much larger than our antenna range length of 2 m. Focusing the array inside the range is therefore technically in the radiative near-field (Fresnel). Near-field measurement can be mathematically transformed to far-field patterns, but the near-field focusing leads to sub-optimal far-field patterns. One solution could be to find far-field phase settings on another location and program the antenna back when placed in the range. However this has proven impractical because the antenna flexibility affects the phase setting. Therefore, the antenna broadside pattern was measured once outside the antenna range in order to verify its pattern and EIRP, and the rest of the measurements, which involve multiple automated iterations of phase steering and flexing shapes, rely on near-field focusing. The steering measurements are mathematically converted to the far field, and therefore the far field plots present small differences from the curve they would have assumed, had the focusing point been placed in the far field. Accuracy remains reasonable. The short focusing distance and limited phase sweeping range also limit the accuracy of directivity calculation. The simulated directivity is ~31 dBi for a 256-element array with a separation of 0.6λ between the elements. While the half-power beam-width of the measurement is nearly identical to simulation, the near-field calculated directivity is only 24 dBi due to significant power in side lobes. The side lobes decay when the result is transformed to far-field, where the calculated directivity improves to 26.5 dBi, as shown in Fig. 7f. Reflection-induced side lobes may not have occurred had the focusing target been placed in the far-field. The remaining difference is probably due to beam widening which is also a result of focusing in the near field Fig. 7.

Figure 7g–j present a variety of RFIC functionality measurements. Figure 7g shows digital control of the output power through the power amplifier cascode voltage. The phase noise performance of the frequency synthesis chain is shown in Fig. 7h. The spectrum is measured through a frequency divider that serves as an amplitude limiter to remove amplitude noise. The first stage PLL contributes 315 fs of rms phase noise and the second stage PLL contributes 420 fs of rms phase noise. The measured total rms phase noise of 530 fs indicates that these sources are adding incoherently as expected and desired. Figure 7i, j are in-array, radiative measurements of current sharing PA stack performance. Figure 7i demonstrates independent phase control of current sharing stacked PAs. In this test two current sharing PAs are turned on and one of them has its second stage PLL phase control settings swept. The interference pattern of the power from both cores is measured by a rectenna array located 20 cm away. If improperly designed or operated, current sharing stacked PAs can become strongly coupled. The presented stacked PAs operate properly, without strong coupling due to on-chip and off-chip capacitive decoupling and sufficient

thermal sinking. This interference measurement demonstrates >360° of phase control as two separate interference peaks are shown. Figure 7j shows a radiated phase noise measurement with one core in a stack on, then a second core in the stack on. Once again, this measurement indicates proper stacked PA operation as the phase noise skirt is not dramatically altered.

### DATA AVAILABILITY

The datasets generated during and/or analysed during the current study are available from the corresponding author on reasonable request.

Received: 13 January 2022; Accepted: 26 September 2022;

Published online: 14 October 2022

### REFERENCES

- Braun, K. F. *Electrical Oscillators and Wireless Telegraphy* (Nobel Lecture, 1909).
- Foster, R. M. Directive diagrams of antenna arrays. *The Bell Syst. Tech. J.* **5**, 292–307 (1926).
- Kear, F. Maintaining the directivity of antenna arrays. *Proce Inst. Radio Eng.* **22**, 847–869 (1934).
- Friis, H. & Feldman, C. A multiple unit steerable antenna for short-wave reception. *Proc. Inst. Radio Eng.* **25**, 841–917 (1937).
- Mailloux, R. *Phased Array Antenna Handbook* 3rd edn (Artech, 2017).
- Bailey, M., Beck, F. & Crosswell, W. Vertically polarized stacked arrays of omnidirectional antennas. *IEEE Trans. Antennas Propag.* **18**, 285–290 (1970).
- Cumming, W. A nonresonant endfire array for vhf and uhf. *IRE Trans. Antennas Propag.* **3**, 52–58 (1955).
- Rotman, W. & Oliner, A. Periodic structures in trough waveguide. *IRE Trans. Microw. Theory Tech.* **7**, 134–142 (1959).
- Ishimaru, A. & Tuan, H.-S. Frequency scanning antennas. *IRE Int. Conv. Record* **9**, 101–109 (1961).
- Spradley, J. A volumetric electrically scanned two-dimensional microwave antenna array. *IRE Int. Conv. Record* **6**, 204–212 (1958).
- Roush, R. & Wiltse, J. Electronically steerable s-band array. *IRE Trans. Antennas Propag.* **9**, 107–109 (1961).
- Donn, C. & Bollesen, A. A 16-element, k-band monolithic active receive phased array antenna. *IEEE AP-S. Int. Symp. Antennas Propag.* **1**, 188–191 (1988).
- Potukuchi, J. et al. MMICs insertion in a ku-band active phased array for communications satellites. *Int. Dig. Microw. Symp.* **2**, 881–884 (1990).
- Moore, G. E. Cramming more components onto integrated circuits, reprinted from electronics, volume 38, number 8, april 19, 1965, pp.114 ff. *IEEE Solid-State Circuits* **11**, 33–35 (2006).
- Bevilacqua, A. & Niknejad, A. An ultrawideband cmos low-noise amplifier for 3.1–10.6-ghz wireless receivers. *IEEE J. Solid-State Circuits* **39**, 2259–2268 (2004).
- Aoki, I., Kee, S., Rutledge, D. & Hajimiri, A. Fully integrated cmos power amplifier design using the distributed active-transformer architecture. *IEEE J. Solid-State Circuits* **37**, 371–383 (2002).
- Simon, K. et al. A production ready, 6-18-ghz, 5-b phase shifter with integrated cmos compatible digital interface circuitry. *IEEE J. Solid-State Circuits* **27**, 1452–1456 (1992).
- Koh, K.-J. & Rebeiz, G. M. 0.13 μm CMOS phase shifters for X-, Ku-, and K-band phased arrays. *IEEE J. Solid-State Circuits* **42**, 2535–2546 (2007).
- von Kaenel, V., Aebischer, D., Piquet, C. & Dijkstra, E. A 320 mhz, 1.5 mw@1.35 v cmos pll for microprocessor clock generation. *IEEE J. Solid-State Circuits* **31**, 1715–1722 (1996).
- Staszewski, R. et al. All-digital pll and transmitter for mobile phones. *IEEE J. Solid-State Circuits* **40**, 2469–2482 (2005).
- Seo, H.-M. et al. A low power fully cmos integrated rf transceiver ic for wireless sensor networks. *IEEE Trans. Very Large Scale Integr. (VLSI) Systems* **15**, 227–231 (2007).
- Jensen, J. C. et al. Single-chip wifi b/g/n 1 × 2 soc with fully integrated front-end amp; pmu in 90nm digital cmos technology. In *2010 IEEE Radio Frequency Integrated Circuits Symposium* 447–450 (IEEE, 2010).
- Winoto, R. et al. A wlan and bluetooth combo transceiver with integrated wlan power amplifier, transmit-receive switch and wlan/bluetooth shared low noise amplifier. In *2012 IEEE Radio Frequency Integrated Circuits Symposium* 395–398 (IEEE, 2012).
- Wang, Y. et al. A 39-ghz 64-element phased-array transceiver with built-in phase and amplitude calibrations for large-array 5 g nr in 65-nm cmos. *IEEE J. Solid-State Circuits* **55**, 1249–1269 (2020).

25. Hajimiri, A., Abiri, B., Bohn, F., Gal-Katziri, M. & Manohara, M. H. Dynamic focusing of large arrays for wireless power transfer and beyond. *IEEE J. Solid-State Circuits* 1–25 (IEEE, 2021).
26. Jang, S., Lu, R., Jeong, J. & Flynn, M. P. A 1-ghz 16-element four-beam true-time-delay digital beamformer. *IEEE J. Solid-State Circuits* **54**, 1304–1314 (2019).
27. Garg, R. et al. 4.3 a 28ghz 4-element mimo beam-space array in 65nm cmos with simultaneous spatial filtering and single-wire frequency-domain multiplexing. In *2020 IEEE Int. Solid-State Circuits Conference-(ISSCC)* 80–82 (IEEE, 2020).
28. Steyskal, H., Shore, R. & Haupt, R. Methods for null control and their effects on the radiation pattern. *IEEE Trans. Antennas Propag.* **34**, 404–409 (1986).
29. Haupt, R. Phase-only adaptive nulling with a genetic algorithm. *IEEE Trans. Antennas Propag.* **45**, 1009–1015 (1997).
30. Poberezhskiy, Y. S. & Poberezhskiy, G. Y. Adaptive spatial hybrid nulling of extremely strong interfering signals. *IEEE Trans. Aerosp. and Electron. Syst.* **57**, 2905–2919 (2021).
31. Hameau, F., Jany, C., Martineau, B., Larie, A. & Mercier, E. A highly linear bidirectional phase shifter based on vector modulator for 60 ghz applications. In *2017 IEEE MTT-S International Microwave Symposium (IMS)* 1707–1710 (IEEE, 2017).
32. Yu, Y. et al. A 60 ghz phase shifter integrated with Ina and pa in 65 nm cmos for phased array systems. *IEEE J. Solid-State Circuits* **45**, 1697–1709 (2010).
33. Cripps, S. *RF Power Amplifiers for Wireless Communications* (Artech House, Boston, 2006).
34. Roupheal, T. *RF and Digital Signal Processing for Software-Defined Radio: A Multi-Standard Multi-Mode Approach* (Newnes, Amsterdam Boston, 2009).
35. Gal-Katziri, M., Ives, C., Khakpour, A. & Hajimiri, A. Optically synchronized phased arrays in cmos. *IEEE J. Solid-State Circuits* **57**, 1578–1593 (2022).
36. Hashemi, M. R. M., Fikes, A. C. & Gal-Katziri, M. et al. A flexible phased array system with low areal mass density. *Nat. Electron.* **2**, 195–205 (2019).
37. Rodenbeck, C. T. et al. Microwave and millimeter wave power beaming. *IEEE J. Microw.* **1**, 229–259 (2021).
38. Abiri, B. et al. A lightweight space-based solar power generation and transmission satellite. *arXiv* <https://arxiv.org/abs/2206.08373> (2022).
39. d'Oliveira, F. A., de Melo, F. C. L. & Devezas, T. C. High altitude platforms—present situation and technology trends. *J. Aerosp. Tech. and Manag.* **1**, 8 (2016).
40. Merhad, K. et al. Cloud-enabled high-altitude platform systems: challenges and opportunities. *Front. Comm. Netw.* <https://doi.org/10.3389/frcmn.2021.716265> (2021).
41. Loughran, J. *Solar-Powered Aircraft Flown for Nearly Three Weeks Without Landing* (The Institution of Engineering and Technology, 2021).
42. Y., Wang et al. All-weather, natural silent speech recognition via machine-learning-assisted tattoo-like electronics. *npj Flex Electron.* <https://doi.org/10.1038/s41528-021-00119-7> (2021).
43. Heinrich, S. et al. Three-dimensional integrated stretchable electronics. *Nat. Electron.* **1**, 473–480 (2018).
44. Terse-Thakoor, T. et al. Thread-based multiplexed sensor patch for real-time sweat monitoring. *npj Flex Electron.* <https://doi.org/10.1038/s41528-020-00081-w> (2020).
45. Z., Zhang et al. Deep learning-enabled triboelectric smart socks for iot-based gait analysis and vr applications. *npj Flex Electron.* <https://doi.org/10.1038/s41528-020-00092-7> (2020).
46. I., Wicaksono et al. A tailored, electronic textile conformable suit for large-scale spatiotemporal physiological sensing in vivo. *npj Flex Electron.* <https://doi.org/10.1038/s41528-020-00092-7> (2020).
47. Y. Jin et al. Identifying human body states by using a flexible integrated sensor. *npj Flex Electron.* <https://doi.org/10.1038/s41528-020-00090-9> (2020).
48. Yuan, H.-C., Ma, Z. & Celler, G. K. Flexible rf/microwave switch-pin diodes using single-crystal si-nanomembranes. In *2007 IEEE/MTT-S International Microwave Symposium* 1027–1030 (IEEE, 2007).
49. Wu, C. et al. A phased array based on large-area electronics that operates at gigahertz frequency. *Nat. Electron.* **4**, 757–766 (2021).
50. Li, W., Vaseem, M., Yang, S. & Shamim, A. Flexible and reconfigurable radio frequency electronics realized by high-throughput screen printing of vanadium dioxide switches. *Microsyst. Nanoeng.* **6**, 77 (2020).
51. Song, C. et al. Advances in wirelessly powered backscatter communications: From antenna/rf circuitry design to printed flexible electronics. *Proc. IEEE* **110**, 171–192 (2022).
52. Gal-Katziri, M. et al. Scalable, deployable, flexible phased array sheets. In *2020 IEEE/MTT-S International Microwave Symposium (IMS)*, 1085–1088 (IEEE, 2020).
53. DuPont. DuPont™ Pyralux-tk®, *Technical Information* [https://sepcu.ru/wp-content/uploads/2018/01/Pyralux\\_TK\\_DataSheet.pdf](https://sepcu.ru/wp-content/uploads/2018/01/Pyralux_TK_DataSheet.pdf) (2015).
54. DuPont. DuPont™ Pyralux-AP®, *Technical Information* [https://www.pragoboard.cz/download/pyralux\\_ap.pdf](https://www.pragoboard.cz/download/pyralux_ap.pdf) (2001).
55. Fikes, A., Mizrahi, O. S. & Hajimiri, A. A framework for array shape reconstruction through mutual coupling. *IEEE Trans. Microw. Theory Tech.* **69**, 4422–4436 (2021).
56. Flexible Circuit Technologies. *Flexible Circuit and Heater Design Guide*. [https://www.flexiblecircuit.com/wp-content/uploads/2015/08/ftc\\_design\\_guide1.pdf](https://www.flexiblecircuit.com/wp-content/uploads/2015/08/ftc_design_guide1.pdf) (2022).
57. P. Bhartia, I. Bahl, R. Garg, A. *Ittipiboon. Microstrip Antenna Design Handbook* (Artech House, 2001).
58. Abiri, B. *Silicon Integrated Arrays: From Microwave to IR* (California Institute of Technology, 2018).
59. NSI-MI. *NSI-MI, Antenna Measurement Systems*. <https://nsi-mi.com/products/system-solutions/near-field-systems/vertical-planar-scanner-systems>. Accessed: 2022-06-29.
60. Balanis, C. A. *Antenna theory 4th edn* (Wiley-Blackwell, 2016).
61. Herd, J. Experimental results from a self-calibrating digital beamforming array. *Int. Symp. Antennas Propag. Soc.* **1**, 384–387 (1990).
62. Lee, K.-M., Chu, R.-S. & Liu, S.-C. A built-in performance-monitoring/fault isolation and correction (pm/fic) system for active phased-array antennas. *IEEE Trans. Antennas Propag.* **41**, 1530–1540 (1993).
63. Ishii, R., Shiramatsu, K., Haruyama, T., Orime, N. & Katagi, T. A built-in correction method of the phase distribution of a phased array antenna. *Antennas Propag. Soc. Symp.* **2**, 1144–1147 (1991).
64. Safaripour, A., Asghari, B. & Hajimiri, A. Proximal-field radiation sensors for millimeter-wave integrated radiators. In *2018 IEEE RFIC* 256–259 (IEEE, 2018).
65. Aumann, H. M., Fenn, A. J. & Willwerth, F. G. Phased array antenna calibration and pattern prediction using mutual coupling measurements. *IEEE Trans. Antennas Propag.* **37**, 844–850 (1989).
66. Fulton, C., Yeary, M., Thompson, D., Lake, J. & Mitchell, A. Digital phased arrays: challenges and opportunities. *Proc. IEEE* **104**, 487–503 (2016).
67. Nawaz, M. I. et al. A review on wideband microstrip patch antenna design techniques. *Int. Conf. Aerosp. Sci. Eng.* <https://doi.org/10.1109/ICASE.2013.6785554> (2013).
68. Khidre, A., Lee, K.-F., Elsherbeni, A. Z. & Yang, F. Wide band dual-beam u-slot microstrip antenna. *IEEE Trans. Antennas Propag.* **61**, 1415–1418 (2013).
69. Rowell, C. & Murch, R. A capacitively loaded pifa for compact mobile telephone handsets. *IEEE Trans. Antennas Propag.* **45**, 837–842 (1997).
70. Wong, H. et al. Small antennas in wireless communications. *Proc. IEEE* **100**, 2109–2121 (2012).
71. Jones, E. & Shimizu, J. A wide-band transverse-slot flush-mounted array. *IRE Trans. Antennas Propag.* **8**, 401–407 (1960).
72. Rogers Corp. *RO3006™ Laminates* <https://rogerscorp.com/advanced-electronics-solutions/ro3000-series-laminates/ro3006-laminates> (2022).
73. Perlmutter, P., Shtrikman, S. & Treves, D. Electric surface current model for the analysis of microstrip antennas with application to rectangular elements. *IEEE Trans. Antennas Propag.* **33**, 301–311 (1985).
74. Visweswaran, A. et al. A 28-nm-cmos based 145-ghz fmcw radar: system, circuits, and characterization. *IEEE J. Solid-State Circuits* **56**, 1975–1993 (2021).
75. Bohn, F., Abiri, B. & Hajimiri, A. Fully integrated cmos x-band power amplifier quad with current reuse and dynamic digital feedback (ddf) capabilities. *IEEE Radio Freq. Integr. Circuits Symp.* <https://doi.org/10.1109/RFIC.2017.7969054> (2017).

## ACKNOWLEDGEMENTS

The authors acknowledge Florian Bohn, Behrooz Abiri, and Amirreza Safaripour for their work developing earlier versions of the RFIC. The authors would also like to acknowledge Mohammed Reza Hashemi for his work on tile-scale array prototypes. The authors would like to thank the Caltech Space Solar Power Project (SSPP) for partial funding of this work. Additionally the authors would like to thank the Rogers Corporations for providing circuit board prototyping materials and Keysight Technologies for providing measurement equipment used in this project.

## AUTHOR CONTRIBUTIONS

The project was conceived by A.H., M.G.-K. and A.F., the array was designed, built, and measured by M.G.-K. and A.F. with input from A.H. All authors contributed to the preparation of this manuscript.

## COMPETING INTERESTS

The authors declare no competing non-financial interests but the following competing financial interests: the authors have filed patents (#20210076159, #20190140349, and several provisional patents) relevant to flexible active arrays.



## ADDITIONAL INFORMATION

**Supplementary information** The online version contains supplementary material available at <https://doi.org/10.1038/s41528-022-00218-z>.

**Correspondence** and requests for materials should be addressed to Matan Gal-Katziri.

**Reprints and permission information** is available at <http://www.nature.com/reprints>

**Publisher's note** Springer Nature remains neutral with regard to jurisdictional claims in published maps and institutional affiliations.



**Open Access** This article is licensed under a Creative Commons Attribution 4.0 International License, which permits use, sharing, adaptation, distribution and reproduction in any medium or format, as long as you give appropriate credit to the original author(s) and the source, provide a link to the Creative Commons license, and indicate if changes were made. The images or other third party material in this article are included in the article's Creative Commons license, unless indicated otherwise in a credit line to the material. If material is not included in the article's Creative Commons license and your intended use is not permitted by statutory regulation or exceeds the permitted use, you will need to obtain permission directly from the copyright holder. To view a copy of this license, visit <http://creativecommons.org/licenses/by/4.0/>.

© The Author(s) 2022